
PREAMBLE

CONTENTS

1 Foundations and Models	1
1.1 The do-it-all Hamiltonian	1
1.2 The Born-Oppenheimer approximation	2
1.3 Density functional theory	3
1.4 Wannier projection	4
1.4.1 Multi-orbital Wannier functions	4
1.4.2 Maximally localized Wannier functions	5
1.5 The multi-orbital Hubbard model	5
1.5.1 Fourier transform of the Coulomb term	6
1.5.2 More symmetries, assumptions and the Kanamori-Hamiltonian	7
1.6 The single-band Hubbard Hamiltonian	9
2 Quantum many-body methods	11
3 Application and Calculation	13
4 Results	15
5 Outlook	17
5.1 Hubbard Model	17

CHAPTER 1

FOUNDATIONS AND MODELS

1.1 The do-it-all Hamiltonian

In the realm of solid state physics, the many-body Schrödinger equation plays a crucial role in understanding the behaviour of electrons in crystalline materials. This equation provides a fundamental framework for describing the quantum mechanical interactions between multiple electrons within a solid. The Schrödinger Hamiltonian for a system consisting of N_{el} electrons and N_{ion} atomic cores — in its full beauty — reads

$$\begin{aligned} \mathcal{H} = & -\frac{\hbar^2}{2M} \sum_i^{N_{\text{ion}}} \nabla_{R_i}^2 - \frac{\hbar^2}{2m} \sum_i^{N_{\text{el}}} \nabla_{r_i}^2 + \frac{1}{2} \sum_{i \neq j}^{N_{\text{ion}}} \frac{Z_i Z_j e^2}{|R_i - R_j|} + \\ & + \frac{1}{2} \sum_{i \neq j}^{N_{\text{el}}} \frac{e^2}{|r_i - r_j|} - \sum_i^{N_{\text{el}}} \sum_j^{N_{\text{ion}}} \frac{Z_j e^2}{|r_i - R_j|} + \mathcal{V}_R, \end{aligned} \quad (1.1)$$

where r_i (R_i) are the positions of the electrons (ions), m (M) their respective masses and Z_i the atomic number of the cores from which the crystal is constructed. The Hamiltonian above can be described in a very simple manner: the first two terms describe the kinetic energy of the ions and electrons, whereas the third and fourth terms denote the mutual Coulomb interaction between all ions and electrons. The second to last term corresponds to the coupling between the ions and electrons and finally \mathcal{V}_R expresses any relativistic effects^[1]. The “only” thing left to do is solve the Schrödinger equation using the Hamiltonian of Eq. (1.1)

$$\mathcal{H}\psi(\{r_i\}, \{R_i\}) = E\psi(\{r_i\}, \{R_i\}), \quad (1.2)$$

which is easier said than done. The primary problem one faces by trying to do exactly that is the sheer number of particles present in a crystalline material. To be more precise, the wavefunction needed to fulfil the eigenvalue equation above would have to depend on all the degrees of freedom of $\mathcal{O}(10^{23})$ electrons and atoms present in solids. The exponential growth in the number of configurations makes it computationally infeasible to directly calculate or even store this quantity, and already a very small number of electrons and atoms $\mathcal{O}(10)$ exceeds the capability of most modern supercomputers. Thus, one goal of condensed matter physicists is not to find the underlying original Hamiltonian but instead to construct approximate models that contain all the physics necessary while still being controllable and numerically feasible.

Usually, approaches to approximate Eq. (1.1) fall into two main categories: (i) using approximate methods to solve the exact Hamiltonian, or (ii) applying (more) exact methods to solve an approximate, mathematically simpler Hamiltonian. Density functional theory (DFT), as an example, falls

^[1]e.g., spin-orbit coupling, relativistic mass correction, anomalous magnetic moments, relativistic Doppler shifts, Zitterbewegung, etc. An instructive example are the relativistic effects that take place in mercury: The binding orbitals of mercury are Lorentz-contracted due to the high speed of the electrons inside these orbitals. This results in a reduction in bonding strength, where ultimately mercury is forming a liquid at room temperatures. In most real solids however, relativistic effects are always negligible and this term will not play a significant role in the majority of calculations.

under the first category, whereas dynamical mean-field theory (DMFT) or the dynamical vertex approximation ($D\Gamma A$) reside in category two. The latter build upon a model Hamiltonian which usually incorporates only a subset of all degrees of freedom, e.g., specific orbitals of atomic shells. In modern calculations, a combination of different tools is used to calculate physical properties of materials. For example, a DFT calculation provides a band structure, where the most relevant orbitals are picked, wherefrom more sophisticated methods, such as DMFT or $D\Gamma A$ can be applied. Within this thesis, we mainly focus on the method of dynamical vertex approximation, however, we will give a short introduction to DFT and DMFT later to complete the spectrum.

1.2 The Born-Oppenheimer approximation

Almost a century ago it was caught that the timescales of the electronic and ionic systems are tremendously different due to their large difference in masses. An electron is around a factor 1800 lighter than a proton. Cores in real solids that contain, e.g., transition metal elements, are five orders of magnitude heavier than electrons. Since relaxation time scales inversely with mass, the electrons usually relax in a much shorter time frame than the ionic cores do, hence one can treat them to be always in the equilibrium position as the cores move through the lattice. This allows us, to a very good approximation, to solve the electronic degrees of freedom for static ionic coordinates. This approximation, called the Born-Oppenheimer approximation, is highly useful in condensed matter physics since it enables the study of electronic band structures, energy levels, and transport properties without the need to explicitly account for the complex interactions between electrons and lattice vibrations induced by the motion of ionic cores. However there are certain phenomena, e.g., conventional phonon-mediated superconductivity, where the coupling of lattice vibrations with electrons can not be neglected. However, there are methods, like perturbation theory, which allow to circumvent this apparent issue. Within the regime of the Born-Oppenheimer approximation, the Hamiltonian of Eq. (1.1) reduces to

$$\mathcal{H}_{B-O} = -\frac{\hbar^2}{2m} \sum_i^{N_{el}} \nabla_{r_i}^2 + \frac{1}{2} \sum_{i \neq j}^{N_{el}} \frac{1}{|r_i - r_j|} + \sum_i^{N_{el}} \mathcal{V}_{ext}(r_i), \quad (1.3)$$

where \mathcal{V}_{ext} describes any external potential, e.g., from ions of the lattice. The other quantities appearing in Eq. (1.3) have already been introduced in Eq. (1.1). This approximation will serve as the basis for all upcoming models if not stated otherwise.

Despite this large simplification, the eigenvalues and the wavefunctions of the Hamiltonian in Eq. (1.3) are still impossible to compute for real-world solids. Most of the difficulties lie in the second term of Eq. (1.3), which describes the Coulomb interaction between pairs of electrons. Due to this mutual electromagnetic interaction, the evolution of every electron is influenced by all other electrons present. Hence all electrons are correlated with each other. In general, these effects are of course not negligible, however in some materials^[2], where the electrons are very mobile, screening effects take place which weaken the Coulomb interaction between the electrons. In this context, a very successful ansatz to make Eq. (1.3) treatable is to model the system as electrons interacting with an effective mean-field generated by all other electrons in its proximity. Such a mean field approach is density functional theory.

^[2]e.g. for most metals

1.3 Density functional theory

The basic idea of density functional theory (DFT) is to work with a simple quantity, i.e., the electron density $\rho(\mathbf{r})$, instead of trying to solve the ab-initio Hamiltonian of Eq. (1.3) - or other, mathematically simpler variants - through complicated many-body wavefunctions. This is possible, at least for the ground state energy and its derivatives, thanks to the two Hohenberg-Kohn theorems, which in essence state that (i) the ground state energy is a unique functional of the electron density $E[\rho(\mathbf{r})]$ (ii) which is minimized at the ground state density $\rho(\mathbf{r}) = \rho_0(\mathbf{r})$. This looks already quite promising, however, DFT lacks in some aspects: firstly, the two H-K theorems do not suggest any constructive/-mathematical way to obtain the energy functional; secondly, this only holds for the ground state density. There is no way to extract any information from excited states; and lastly, the $3N$ -dimensional object $\psi(\{\mathbf{r}_i\})$ is compressed into a three-dimensional object $\rho(\mathbf{r})$. Consequently, an arbitrarily tiny variation in $\rho(\mathbf{r})$ might correspond to a huge change in $E[\rho(\mathbf{r})]$.

The big question is: "How does one approximate the energy functional $E[\rho(\mathbf{r})]?$ ". To answer this, we start with splitting up the energy functional to distinguish different contributions,

$$E[\rho(\mathbf{r})] = T[\rho(\mathbf{r})] + E_H[\rho(\mathbf{r})] + \int d^3r \rho(\mathbf{r})V(\mathbf{r}) + E_{XC}[\rho(\mathbf{r})]. \quad (1.4)$$

Here, $T[\rho(\mathbf{r})]$ is the kinetic energy of the electrons. Computing this often turns out to be very challenging. $E_H[\rho(\mathbf{r})]$ is the electrostatic energy (inter alia self-interaction of electrons), given by the Hartree-term

$$E_H[\rho(\mathbf{r})] = \frac{1}{2} \int d^3r \int d^3r' \frac{\rho(\mathbf{r})\rho(\mathbf{r}')}{|\mathbf{r} - \mathbf{r}'|}. \quad (1.5)$$

The potential term includes energies of electrons in external potentials (e.g., nuclei) and is usually not hard to calculate. Lastly, $E_{XC}[\rho(\mathbf{r})]$ includes everything else, i.e., the exchange and correlation energies. Dealing with the potential and the Hartree-term is easy compared to the treatment of the kinetic and exchange/correlation functional. There are many ways to construct the kinetic and XC functionals. The most frequently used framework to include the main contribution to the kinetic energy functional is Kohn-Sham DFT and exchange/correlation functionals can be obtained by the local density approximation (LDA) or higher-order variants within K-S DFT, such as different flavours of generalized gradient approximations (GGA). Stepping higher on Jacob's ladder^[3], more sophisticated methods are hyper-GGA or several variants of (range-separated) hybrid functionals.

This already sounds very promising, why should we not stop here and solely describe our metals with DFT? This apparent question can be answered very straightforwardly: increased localization of d or f orbitals and increased correlation effects therein. Since orbitals with higher angular momentum are more localized in real space, electronic densities in those orbitals are higher and consequently, the electrons within those orbitals are more correlated. Consequently, screening of other itinerant electrons is, in a way, suppressed. Therefore, since DFT is a mean-field approach and relies on the concept of screening, it is not very successful in describing those systems. For example, DFT predicts a metallic behaviour in partially filled 3d transition metal or 4f rare-earth elements, whereas experiments find them to be insulating. Thus, for strongly correlated materials, sophisticated many-body

^[3]Refers to a hierarchical classification of density functional approximations (DFAs) used in Kohn-Sham density functional theory (DFT). The ladder represents a sequence of increasingly accurate and complex approximations for the exchange-correlation energy, which is a key component of the total energy in DFT. Jacob's Ladder begins with the simplest and least accurate approximations at the lower rungs and progresses towards more sophisticated and accurate methods at the higher rungs. Each rung represents a level of approximation that includes additional physical effects and improves upon the previous level.

methods, which do not approximate the Born-Oppenheimer Hamiltonian of Eq. (1.3), are needed. However, since all many-body techniques are numerically expensive, a straightforward application to the Hamiltonian of Eq. (1.3) is not feasible, thus model Hamiltonians, such as the Hubbard Hamiltonian — the modern standard Hamiltonian of strongly correlated condensed matter systems, which is described in Sec. 1.5 — are needed.

1.4 Wannier projection

Within DFT+others^[4] approach, a Wannier projection is used to develop localized wavefunctions, also called Wannier functions, from extended Bloch wavefunctions used in DFT. These localized Wannier functions are created for the correlated orbitals and are then interpreted as the localized orbitals of multi-orbital models, such as the Hubbard model, which will be discussed later in Sec. 1.5.

The eigenstates of the Schrödinger equation in a periodic lattice are Bloch functions of the form

$$\psi_{n\mathbf{k}}(\mathbf{r}) = e^{i\mathbf{k}\mathbf{r}} u_n(\mathbf{r}), \quad (1.6)$$

where $u_n(\mathbf{r} + \mathbf{R}) = u_n(\mathbf{r})$ incorporates the periodicity of the lattice and n denotes the band index. To obtain a local set of basis functions, one applies a Fourier transform to the Bloch functions,

$$w_{n\mathbf{R}}(\mathbf{r}) = \frac{1}{\sqrt{N}} \sum_{\mathbf{k} \in \text{BZ}} e^{-i\mathbf{k}\mathbf{R}} \psi_{n\mathbf{k}}(\mathbf{r}), \quad (1.7)$$

where \mathbf{R} is a lattice vector and $w_{n\mathbf{R}}(\mathbf{r})$ is a Wannier function centred around the lattice site \mathbf{R} . Wannier functions are an equivalent basis in band-space compared to the Bloch functions, however they are not eigenstates of the lattice Hamiltonian. Therefore, in a way, de-localization in energy is what compensates for localization in real space. Additionally, the choice for Eq. (1.7) is not unique, since the Bloch functions have a gauge freedom of a unitary transformation — similar to a basis transformation — which reads

$$\psi_{n_1\mathbf{k}}(\mathbf{r}) = \sum_{n_2} U_{n_1 n_2}^{\mathbf{k}} \psi_{n_2\mathbf{k}}(\mathbf{r}), \quad (1.8)$$

where $U_{n_1 n_2}^{\mathbf{k}}$ is a unitary matrix, mixing orbitals n_1 and n_2 at each point in \mathbf{k} -space. Consequently, there is some degree of freedom to Wannier function construction, which can be applied to the creation of maximally localized Wannier functions, for example.

1.4.1 Multi-orbital Wannier functions

So far, we assumed a single isolated band with band index n . This does not capture real-world materials, where one usually has a “spaghetti” of many bands that overlap and hybridize with each other. Let us assume that the number of Bloch bands, which are encompassed in the Wannier projection, is L and these bands are separated by all other bands present. In this case, the transformation of Eq. (1.8) can be generalized to

$$\tilde{\psi}_{m\mathbf{k}}(\mathbf{r}) = \sum_{n=1}^L U_{mn}^{\mathbf{k}} \psi_{n\mathbf{k}}(\mathbf{r}), \quad (1.9)$$

^[4]“Others” being, e.g., DMFT, GW or DΓA.

where $U_{mn}^k \in L \times L$. The construction of the Wannier functions follows

$$\psi_{mR}(\mathbf{r}) = \sum_{\mathbf{k} \in BZ} e^{-ikR} \sum_{n=1}^L U_{mn}^k \psi_{nk}(\mathbf{r}), \quad (1.10)$$

which allows for an additional mixing of the Bloch states. In this case, the unitary matrix U_{mn}^k encodes the gauge freedom of the Wannier projection. A popular unique “gauge fixing” of U_{mn}^k is through maximally localized Wannier functions.

1.4.2 Maximally localized Wannier functions

The idea here is to choose U_{mn}^k such that the sum of quadratic spreads of the Wannier functions is minimized. This spread of the set of L Wannier functions in real space is quantified by the localization functional Ω and reads

$$\Omega = \sum_m \left[\langle \mathbf{r}^2 \rangle_m - \langle \mathbf{r} \rangle_m^2 \right] = \sum_m \left[\langle \psi_{mR} | \mathbf{r}^2 | \psi_{mR} \rangle - |\langle \psi_{mR} | \mathbf{r} | \psi_{mR} \rangle|^2 \right]. \quad (1.11)$$

Applying a minimization procedure to the spread of Wannier functions results in a “gauge-fixed” \tilde{U}_{mn}^k , choosing the unitary transformation uniquely.

1.5 The multi-orbital Hubbard model

Now we have acquired enough tools to describe the “standard model” of strongly correlated electron systems. The development of this model dates back to more than a century. As already discussed at the end of Sec. 1.3, for elements with partially filled d or f orbitals, a mean-field description, as is the basis for DFT calculations, is not enough to successfully describe microscopic and macroscopic phenomena due to strong electronic correlation. On the other hand, a treatment beyond mean-field of the Born-Oppenheimer Hamiltonian of Eq. (1.3) is currently not possible. Hence, the method of choice is the introduction of a mathematically simpler, but conceptually still very relevant model Hamiltonian, which successfully captures the physical essence of condensed matter. As a result, the Hamiltonian - named for J. Hubbard - was developed.

As a starting point we choose the Hamiltonian of Eq. (1.3) in second quantization

$$\begin{aligned} \mathcal{H} = & \sum_{\sigma} \int d^3r \hat{\Psi}_{\sigma}^{\dagger}(\mathbf{r}) \left[-\frac{\hbar^2}{2m} \nabla_{\mathbf{r}}^2 + V(\mathbf{r}) \right] \hat{\Psi}_{\sigma}(\mathbf{r}) \\ & + \frac{1}{2} \sum_{\sigma\sigma'} \int d^3r \int d^3r' \hat{\Psi}_{\sigma}^{\dagger}(\mathbf{r}) \hat{\Psi}_{\sigma'}^{\dagger}(\mathbf{r}') \frac{e^2}{|\mathbf{r} - \mathbf{r}'|} \hat{\Psi}_{\sigma'}(\mathbf{r}') \hat{\Psi}_{\sigma}(\mathbf{r}), \end{aligned} \quad (1.12)$$

where $\hat{\Psi}_{\sigma}^{(\dagger)}(\mathbf{r})$ are field operators that annihilate (create) an electron with spin σ at position \mathbf{r} . We can expand these field operators in terms of maximally localized Wannier functions introduced in Sec. 1.4.2, yielding

$$\hat{\Psi}_{\sigma}^{(\dagger)}(\mathbf{r}) = \sum_{R,m} w_{mR}^{(*)} \hat{c}_{Rm\sigma}^{(\dagger)}, \quad (1.13)$$

where w_{mR} is the (maximally localized) Wannier function of orbital m centred around R , and $\hat{c}_{Rm\sigma}$ the corresponding annihilation operator. Note that the orbitals m are usually the localized 3d or 4f

orbitals in transition metals or rare earth elements. With the help of Eq. (1.13), the Hamiltonian of Eq. (1.12) can be rewritten as

$$\begin{aligned} \mathcal{H} = & - \sum_{\substack{\mathbf{R}\mathbf{R}' \\ mm',\sigma}} t_{mm'}(\mathbf{R}, \mathbf{R}') \hat{c}_{\mathbf{R}m\sigma}^\dagger \hat{c}_{\mathbf{R}'m'\sigma} \\ & + \frac{1}{2} \sum_{\substack{\mathbf{R}_1 \mathbf{R}_2 \mathbf{R}_3 \mathbf{R}_4 \\ ll'mm' \\ \sigma\sigma'}} U_{lm'ml'}(\mathbf{R}_1, \mathbf{R}_2, \mathbf{R}_3, \mathbf{R}_4) \hat{c}_{\mathbf{R}_3 m' \sigma}^\dagger \hat{c}_{\mathbf{R}_1 l \sigma'}^\dagger \hat{c}_{\mathbf{R}_2 m \sigma'} \hat{c}_{\mathbf{R}_4 l' \sigma}, \end{aligned} \quad (1.14)$$

where $ll'mm'$ denote different Wannier orbitals, while \mathbf{R}_i corresponds to a lattice site. Hence, the first term in the Hubbard Hamiltonian represents the kinetic energy part and describes electrons hopping from orbital m' at \mathbf{R}' to orbital m at \mathbf{R} , possibly changing spin in the process. The probability of the hopping to occur is given by the hopping matrix $t_{mm'}(\mathbf{R}, \mathbf{R}')$. The second term in Eq. (1.14) encodes the Coulomb interaction between two electrons. A couple terms of the multi-orbital Hubbard Hamiltonian are visually depicted in Fig. 1.1, where a subset of effects of $t_{mm'}(\mathbf{R}, \mathbf{R}')$ and $U_{lm'ml'}(\mathbf{R}_1, \mathbf{R}_2, \mathbf{R}_3, \mathbf{R}_4)$ are shown for two lattice sites. For brevity, the hopping matrix $t_{mm'}(\mathbf{R}, \mathbf{R}')$

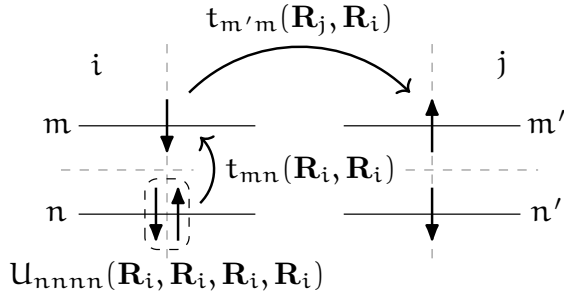


FIGURE 1.1: Visual representation of a subset of interaction and hopping terms of Eq. (1.14). We show two lattice sites i and j with orbitals m , n and m' , n' , respectively.

and Coulomb interaction $U_{lm'ml'}(\mathbf{R}_1, \mathbf{R}_2, \mathbf{R}_3, \mathbf{R}_4)$ are given by

$$t_{mm'}(\mathbf{R}, \mathbf{R}') = - \int d^3r w_{m\mathbf{R}}^*(\mathbf{r}) \left[-\frac{\hbar^2}{2m} \nabla_{\mathbf{r}}^2 + V(\mathbf{r}) \right] w_{m'\mathbf{R}'} \quad \text{and} \quad (1.15)$$

$$U_{lm'ml'}(\mathbf{R}_1, \mathbf{R}_2, \mathbf{R}_3, \mathbf{R}_4) = \int d^3r \int d^3r' w_{m'\mathbf{R}_3}^*(\mathbf{r}) w_{l\mathbf{R}_1}^*(\mathbf{r}') \frac{e^2}{|\mathbf{r} - \mathbf{r}'|} w_{m\mathbf{R}_2}(\mathbf{r}') w_{l'\mathbf{R}_4}(\mathbf{r}). \quad (1.16)$$

While for Eq. (1.14) we have already restricted ourselves to a subspace of orbitals, it is still too complex to be solved exactly in the general case. The complexity can be further reduced by either placing further assumptions and restrictions or by using symmetries of the Hamiltonian, which are present in the hopping and interaction terms. Note, that Eq. (1.16) overestimates the repulsive Coulomb interaction since screening effects from electrons outside the orbital subspace are not considered. One way to partly overcome this issue is proposed in the constrained Random Phase Approximation (cRPA). For details on how cRPA works, we refer the reader to [AAFAHJKDFHKLJSDBNFKJSB].

1.5.1 Fourier transform of the Coulomb term

For reasons that become apparent later, it is more convenient to express the interaction term in Fourier space for diagrammatic calculations. The real-space interaction term in Eq. (1.14) inherently depends

on four lattice vectors. However, to simplify the notation, one of these arguments (e.g., \mathbf{R}_4) can be eliminated by expressing the distances relative to the lattice site 4 rather than using their absolute positions. Therefore,

$$\hat{U} = \frac{1}{2} \sum_{\substack{\mathbf{R}_1 \mathbf{R}_2 \mathbf{R}_3 \\ ll' mm' \\ \sigma \sigma'}} U_{lm'ml'}(\mathbf{R}_1, \mathbf{R}_2, \mathbf{R}_3) \hat{c}_{R_3 m' \sigma}^\dagger \hat{c}_{R_1 l \sigma'}^\dagger \hat{c}_{R_2 m \sigma'} \hat{c}_{0l' \sigma}. \quad (1.17)$$

This quantity naturally fulfils a swapping symmetry, where the simultaneous exchange of both incoming and outgoing particles keeps it invariant, i.e.,

$$U_{lm'ml'}(\mathbf{R}_1, \mathbf{R}_2, \mathbf{R}_3) = U_{m'l'l'm}(\mathbf{R}_3 - \mathbf{R}_2, -\mathbf{R}_2, \mathbf{R}_1 - \mathbf{R}_2). \quad (1.18)$$

The general Fourier transform of the tensor in Eq. (1.17) with respect to the lattice positions \mathbf{R}_i yields

$$U_{lm'ml'}^{qkk'} = \sum_{\mathbf{R}_1 \mathbf{R}_2 \mathbf{R}_3} e^{ik\mathbf{R}_1} e^{-i(k-q)\mathbf{R}_2} e^{-i(k'-q)\mathbf{R}_3} U_{lm'ml'}(\mathbf{R}_1, \mathbf{R}_2, \mathbf{R}_3), \quad (1.19)$$

or for the full interaction operator in Eq. (1.14)

$$\hat{U} = \frac{1}{2} \sum_{\substack{qkk' \\ ll' mm' \\ \sigma \sigma'}} U_{lm'ml'}^{qkk'} \hat{c}_{k'-q m' \sigma}^\dagger \hat{c}_{kl \sigma'}^\dagger \hat{c}_{k-q m \sigma'} \hat{c}_{k'l' \sigma}, \quad (1.20)$$

where the Fourier transforms of the creation and annihilation operators are given by

$$\hat{c}_{kl \sigma}^{(\dagger)} = \sum_{\mathbf{R}} e^{(-)ik\mathbf{R}} \hat{c}_{Rl \sigma}^{(\dagger)}. \quad (1.21)$$

One potential simplification to consider here is neglecting orbital overlap of neighbouring sites, pairing up the operators at sites $\mathbf{0}$ and \mathbf{R} . This eliminates the \mathbf{k} -point dependence of the Coulomb operator and thus

$$U_{lm'ml'} \equiv U_{lm'ml'}(\mathbf{0}, \mathbf{0}, \mathbf{0}), \quad \text{and} \quad (1.22)$$

$$V_{lm'ml'}^q \equiv \sum_{\mathbf{R} \neq \mathbf{0}} e^{iq\mathbf{R}} U_{lm'ml'}(\mathbf{R}, \mathbf{R}, \mathbf{0}), \quad (1.23)$$

corresponding to a purely local interaction $U_{lm'ml'}$ and a purely non-local interaction $V_{lm'ml'}^q$. In this case the exchange symmetry of the incoming and outgoing electron reduces to $U_{lm'ml'} = U_{m'l'l'm}$ and $V_{lm'ml'}^q = V_{m'l'l'm}^{-q}$.

1.5.2 More symmetries, assumptions and the Kanamori-Hamiltonian

cRPA is a framework in which all interaction combinations for $U_{lm'ml'}(\mathbf{R}_1, \mathbf{R}_2, \mathbf{R}_3, \mathbf{R}_4)$ can be computed, however there are certain symmetries and assumptions that help reduce the amount of individual elements of $U_{lm'ml'}(\mathbf{R}_1, \mathbf{R}_2, \mathbf{R}_3, \mathbf{R}_4)$ drastically. Similar simplifications can be made for the kinetic term in Eq. (1.14). Previously, it was stated that due to the localized nature of Wannier orbitals, the Hopping amplitudes reduce (rapidly) in magnitude the further the orbitals are located in real space due to reduced orbital overlap. The decay of $t_{mm'}(\mathbf{R}, \mathbf{R}')$ is roughly proportional to $|\mathbf{R} - \mathbf{R}'|^{-1}$. Hence for practical calculations, a very good approximation can be achieved by considering only the three

closest (in distance) hopping terms: nearest (t), next-nearest (t'); and next-next-nearest (t'') neighbor, see Fig. 1.3 for an illustration. Elements of $U_{lm'm'l'}(\mathbf{R}_1, \mathbf{R}_2, \mathbf{R}_3, \mathbf{R}_4)$ usually decay even faster than the hopping terms due to the integral over four orbitals in Eq. (1.16) compared to two. Aside from this argument, further assumptions about the interaction can be made: (i) the Wannier functions respect SU(2) symmetry; (ii) the Wannier functions of the subset of orbitals preserve orbital symmetry; and (iii) the Coulomb interaction of electrons on different lattice sites is small compared to the on-site Coulomb interaction, e.g., $U_{lm'm'l'}(\mathbf{R}, \mathbf{R}, \mathbf{R}, \mathbf{R}) \gg U_{lm'm'l'}(\mathbf{R}, \mathbf{R}, \mathbf{R}, \mathbf{R}') \gg U_{lm'm'l'}(\mathbf{R}, \mathbf{R}, \mathbf{R}', \mathbf{R}'')$. Let us briefly justify these assumptions: (i) holds when spin-orbit coupling is ignored, the material is in the paramagnetic phase, and no external electromagnetic fields are applied; (ii) applies to degenerate orbital subsets, like the t_{2g} and e_g orbitals in the 3d shell; and (iii) is valid as long as the Wannier functions remain localized around their respective lattice sites, which is generally true for d or f shells. Under the assumptions (i)-(iii) $U_{lm'm'l'}(\mathbf{R}_1, \mathbf{R}_2, \mathbf{R}_3, \mathbf{R}_4)$ is constrained to a single lattice site and has only three independent entries, commonly denoted by the intra-orbital and inter-orbital interactions U and U' , respectively, and the Hund's exchange J . A visual representation of the effects of U , U' and J can be found in Fig. 1.2. These quantities are given by

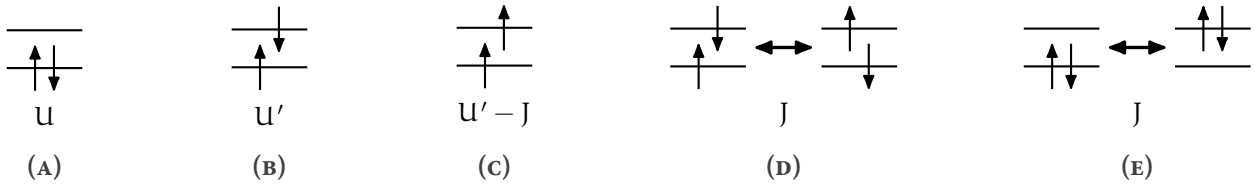


FIGURE 1.2: Kanamori parameters U , U' and J as described in the text: (A) intra-orbital Coulomb interaction, (B)-(C) inter-orbital Coulomb interaction, (D) spin-flip of an electron pair and (E) pair hopping.

$$U = U_{llll} = \int d^3r \int d^3r' |w_l(\mathbf{r})|^2 V_c(\mathbf{r} - \mathbf{r}') |w_l(\mathbf{r}')|^2, \quad (1.24)$$

$$U' = U_{llmm} = \int d^3r \int d^3r' |w_l(\mathbf{r})|^2 V_c(\mathbf{r} - \mathbf{r}') |w_m(\mathbf{r}')|^2 \quad \text{and} \quad (1.25)$$

$$J = U_{lmm'l} = \int d^3r \int d^3r' w_l^*(\mathbf{r}) w_m^*(\mathbf{r}') V_c(\mathbf{r} - \mathbf{r}') w_l(\mathbf{r}') w_m(\mathbf{r}), \quad (1.26)$$

where $V_c(\mathbf{r} - \mathbf{r}')$ is the screened Coulomb interaction term. For cubic symmetry - due to constraint (ii) - there are only two independent quantities for the interaction U , resulting in $U' = U - 2J$. With the help of these three parameters we can simplify the Hamiltonian of Eq. (1.14) and for the general case the so-called Kanamori-Hamiltonian reads

$$\begin{aligned} \mathcal{H}_{\text{Kanamori}} = & - \sum_{\substack{\mathbf{R}\mathbf{R'} \\ mm',\sigma}} t_{mm'}(\mathbf{R}, \mathbf{R}') \hat{c}_{\mathbf{R}m\sigma}^\dagger \hat{c}_{\mathbf{R}'m'\sigma} \\ & + U \sum_{\mathbf{R}, l} \hat{n}_{\mathbf{R}l\uparrow} \hat{n}_{\mathbf{R}l\downarrow} + \sum_{\substack{\mathbf{R}, l \neq m \\ \sigma\sigma'}} (U' - J\delta_{\sigma\sigma'}) \hat{n}_{\mathbf{R}l\sigma} \hat{n}_{\mathbf{R}m\sigma'} \\ & - J \sum_{\mathbf{R}, l \neq m} \hat{c}_{\mathbf{R}l\uparrow}^\dagger \hat{c}_{\mathbf{R}l\downarrow} \hat{c}_{\mathbf{R}m\downarrow}^\dagger \hat{c}_{\mathbf{R}m\uparrow} + J \sum_{\mathbf{R}, l \neq m} \hat{c}_{\mathbf{R}l\uparrow}^\dagger \hat{c}_{\mathbf{R}l\downarrow}^\dagger \hat{c}_{\mathbf{R}m\downarrow} \hat{c}_{\mathbf{R}m\uparrow}, \end{aligned} \quad (1.27)$$

where $\hat{n}_{l\sigma}$ is the number operator ($\hat{c}_{l\sigma}^\dagger \hat{c}_{l\sigma}$) that counts the number of electrons in orbital l with spin σ . The Kanamori Hamiltonian is a widely used model for strongly correlated systems and it can capture

a lot of physics despite its rather crude approximations. Today, the Kanamori Hamiltonian is mostly used not only to describe spin and orbital order, including magnetically ordered phases in materials with partially filled d or f shells, but also to capture a variety of Mott-insulating states, where strong on-site electron repulsion causes electron localization.

1.6 The single-band Hubbard Hamiltonian

The most widely used model Hamiltonian to describe strongly correlated materials is the one-band Hubbard model. It is the single-orbital version of the Kanamori Hamiltonian and reads

$$\mathcal{H}_{\text{Hubbard}} = - \sum_{i \neq j, \sigma} t_{ij} \hat{c}_{i\sigma}^\dagger \hat{c}_{j\sigma} + U \sum_i \hat{n}_{i\uparrow} \hat{n}_{i\downarrow} - \mu \sum_i (\hat{n}_{j\uparrow} + \hat{n}_{j\downarrow}), \quad (1.28)$$

where i and j denote the lattice site in the N -dimensional lattice and the hopping is spin-independent. The interaction U is purely local and $\mu = t_{ii}$ is the chemical potential. Due to the reduction to a single orbital, the interaction terms U' and J do not exist any more as they used to incorporate different orbitals. This is one of the simplest forms of the most general Hubbard Hamiltonian of Eq. (1.14), however it can still not be solved exactly since the kinetic term is diagonal in momentum space whereas the interaction term is diagonal in real space. A general analytical solution to the model does therefore not exist, however recent advances allowed numerical calculations to exactly calculate the eigendecomposition of the Hubbard Hamiltonian for a couple different parameter sets. To visually illustrate the model's description, a representation of the hopping and interaction terms of Eq. (1.28) can be seen in Fig. 1.3.

The very extreme simplification of the Hubbard model is called the Hubbard Atom and it represents an isolated lattice site with either zero, one or two electrons occupying a single orbital interacting through the instantaneous electrostatic repulsion U . It is also often coined “atomic limit”, because it can be formulated as a limiting case for the Hubbard model where all hopping amplitudes are set to zero. The Hubbard Atom is solvable with analytical methods and can already give a lot of information about non-perturbative processes in condensed matter physics.

In the last chapter, we looked at the fundamental Hamiltonians and a few specific models that create the theoretical foundation for modelling strongly correlated electron systems, such as transition metal oxides (e.g., manganites, cuprates or nickelates), heavy fermion systems (e.g., compounds containing rare-earth or actinide elements), Mott insulators (e.g., V_2O_3) and many more. We have developed the fundamental ideas required to explain the distinctive behaviour of particles in systems where interactions play an important role.

With this framework in place, we now proceed to introduce the mathematical tools required to perform calculations within these models. The next two chapters present a detailed toolkit, including many-body Green's functions and diagrammatic methods, such as dynamical mean-field theory (DMFT) or the dynamical vertex approximation D Γ A. These approaches ready us to translate the abstract models into concrete results, allowing for the computation of observables and the quantitative study of strongly correlated systems. This toolkit will be essential for extracting physical insights from the models we have discussed and for bridging theory with experimental observations in the field.

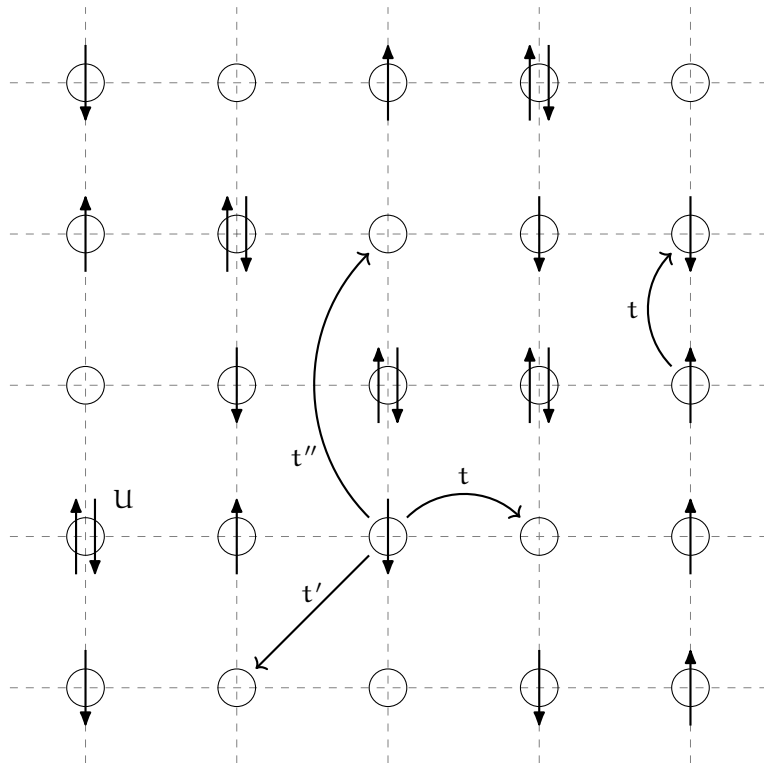


FIGURE 1.3: Visual representation of the two-dimensional square lattice Hubbard model. Each lattice site either contains zero, one or two electrons. Every circle represents a local orbital at any site. Here, t , t' and t'' denote nearest-neighbour hopping, next-nearest-neighbour hopping and next-next-nearest-neighbour hopping, respectively. Reasonable values for t , t' , t'' and U are obtained from density functional theory (DFT) calculations [PavariniE2001BTiH] or extracted from ARPES studies [HashimotoM2008Deot]. For e.g., cuprates, one finds that $t \approx 0.3\text{-}0.5$ eV, $t' \approx -0.2t$, $t'' \approx 0.1t$ and $U \approx 8t$.

CHAPTER 2

QUANTUM MANY-BODY FRAMEWORK

This chapter is dedicated to introducing the necessary tools needed to perform realistic material calculations using DMFT or D Γ A. We start with the most central objects - the Green's functions - and subsequently assemble a complete framework which enables us to calculate a number of physical properties, e.g. the susceptibility, optical conductivity, superconductivity, pseudogaps and more, that stem from the correlated interplay between electrons or holes.

2.1 One-particle Green's functions

Green's functions are fundamental tools in many-body physics, used to study the properties and behavior of interacting quantum systems. These mathematical objects encode information about the propagation of particles or excitations within a system and serve as the cornerstone for analyzing both equilibrium and nonequilibrium states. In the many-body regime, Green's functions extend beyond single-particle descriptions to include complex interactions among multiple particles. They provide insights into phenomena such as quasiparticle lifetimes, collective excitations and response functions. Specifically, one- and two-particle Green's functions describe the propagation of a single particle and the correlated motion of particle pairs, respectively. Alongside of the mathematical description of Green's function-based expressions, we also provide a pictorial description of the equations using Feynman diagrams. These Feynman diagrams allow us to easily describe interaction processes visually. Lines and vertices within the diagrams indicate particle propagators and interaction vertices, respectively. External legs will be coloured gray while inner legs and interaction lines will be coloured black.

In condensed matter physics, we are only interested in finite-temperature effects. Hence it is practical to use the so-called Matsubara formalism[T. Matsubara. “A new approach to quantum-statistical mechanics”] in imaginary time by performing a Wick rotation $t \rightarrow -i\tau$ [G. C. Wick. “Properties of Bethe-Salpeter Wave Function”. Furthermore, most many-body quantities described in the following are n -point (correlation) functions^[1]. These functions typically include a subset of the following parameters for each external leg: (Matsubara) frequency (ν), spin index (σ), orbital index (o), lattice position (R), momentum (k) or imaginary time (τ). This introduces a huge amount of dependencies appended to a variable and can be very cumbersome to read through if explicitly written down. Therefore, to increase readability, we follow Ref. [N. E. Bickers and D. J. Scalapino. “Conserving approximations ...”] and group all indices that are not explicitly written down into a compound index, e.g. $i = \{o_i, \sigma_i, R_i\}$. If an equation containing spatial or momentum-dependent quantities is written down with a compound index, it applies equally in both real and Fourier space. Furthermore, summing over these compound indices means summing over all individual components they include, with a normalization of $\frac{1}{\beta}$ for frequency sums and $\frac{1}{N_k}$ for momentum sums, where $\beta = \frac{1}{k_B T}$ is the inverse temperature and N_k is the total number of reciprocal lattice points.

After this short introduction, let us dive in by defining the most central quantity, the two-point (one-

^[1]Here, n denotes the number of “external legs” of the corresponding Feynman diagram.

particle) Green's function, in a system in thermal equilibrium as

$$G_{12}^k = -\langle \mathcal{T} [\hat{c}_{k,1} \hat{c}_{k,2}^\dagger] \rangle, \quad (2.1)$$

where $\hat{c}_{k,i}$ ($\hat{c}_{k,i}^\dagger$) are fermionic annihilation (creation) operators which annihilate (create) an electron with parameters $i = \{\sigma_i, o_i, \tau_i\}$ and momentum k in the system. $\langle \cdot \rangle = \frac{1}{Z} \text{Tr} \{e^{-\beta \hat{H}} \cdot\}$ with $Z = \text{Tr} \{e^{-\beta \hat{H}}\}$ describes the thermal expectation value. Note, that the time evolution operator $e^{i\hat{H}\tau} = e^{\hat{H}\tau}$ is real after performing the Wick rotation to imaginary time and the Boltzmann weight $e^{\beta \hat{H}}$ describes nothing more than an additional evolution in imaginary time. Lastly, $\mathcal{T}[\cdot]$ is the imaginary time ordering operator, where

$$\mathcal{T} [\hat{c}_1^{(\dagger)}(\tau_1) \hat{c}_2^{(\dagger)}(\tau_2)] = \Theta(\tau_1 - \tau_2) \hat{c}_1^{(\dagger)}(\tau_1) \hat{c}_2^{(\dagger)}(\tau_2) - \Theta(\tau_2 - \tau_1) \hat{c}_2^{(\dagger)}(\tau_2) \hat{c}_1^{(\dagger)}(\tau_1). \quad (2.2)$$

The Green's function measures the probability amplitude of a propagation process and reads as a Feynman diagram

$$G_{12} = \bullet^1 \xrightarrow{} \bullet^2.$$

FIGURE 2.1: Diagrammatic representation of the one-particle Green's function G_{12} . The electron is annihilated at 1, propagates in imaginary time from τ_1 to τ_2 and is created at 2.

In homogeneous systems, e.g., infinite or translationally invariant systems, the Green's function inherits the system's properties and becomes invariant under spatial translations. This means that $G_{12}(R_1, R_2) = G_{12}(R_1 - R_2, 0) = G_{12}(R)$. In Fourier space, this means that the Green's function is also only dependent on a single momentum parameter, $G_{12}(k_1, k_2) = G_{12}(k_1 - k_2, 0) = G_{12}(k)$. Furthermore, if the system is stationary, i.e., the Hamiltonian is not explicitly dependent on imaginary time, then $G_{12}(\tau_1, \tau_2) = G_{12}(\tau_1 - \tau_2, 0) = G_{12}(\tau)$. In absence of spin-orbit coupling, the spins at 1 and 2 need to be equal and therefore G_{12} only depends on a single spin component. Additionally, the *fermionic* Green's function can be shown to be anti-periodic in imaginary time with a period of β ^[2],

$$G_{12}(\tau) = -G_{12}(\beta - \tau) \quad \text{for } \tau > 0 \text{ and} \quad (2.3a)$$

$$G_{12}(\tau) = -G_{12}(\beta + \tau) \quad \text{for } \tau < 0. \quad (2.3b)$$

This anti-periodicity in time leads to the Fourier transform to be defined over a discrete set of imaginary frequencies, the so-called Matsubara frequencies, which for fermionic quantities are given by $\nu_n = (2n+1)\frac{\pi}{\beta}$. In contrast, *bosonic* Green's functions are periodic in imaginary time with period β and therefore the Fourier transform includes the set of bosonic Matsubara frequencies $\omega_n = (2n)\frac{\pi}{\beta}$. In the following, we will always denote fermionic Matsubara frequencies with ν_n and bosonic ones with ω_n . The fermionic- and bosonic-like Fourier transforms of $G_{12}(\tau)$ become, respectively,

$$G_{12}(i\nu_n) = \int_0^\beta d\tau G_{12}(\tau) e^{i\nu_n \tau} \quad \text{and} \quad G_{12}(i\omega_n) = \int_0^\beta d\tau G_{12}(\tau) e^{i\omega_n \tau} \quad (2.4)$$

and only require the knowledge of Green's functions for positive imaginary times τ . The inverse Fourier transforms are given by

$$G_{12}(\tau) = \frac{1}{\beta} \sum_n G_{12}(i\nu_n) e^{-i\nu_n \tau} \quad \text{and} \quad G_{12}(\tau) = \frac{1}{\beta} \sum_n G_{12}(i\omega_n) e^{-i\omega_n \tau}. \quad (2.5)$$

^[2]This originates from the Boltzmann term $e^{\beta \hat{H}}$ in the thermal expectation value and restricts the imaginary time domain to $\tau \in [-\beta, \beta]$.

If we perform a spectral representation of the fermionic Green's function in Eq. (??) and calculate the discrete Fourier transform, we find that

$$G_{12}(iv_n) = \frac{1}{Z} \sum_{mn} (e^{-\beta E_m} + e^{-\beta E_n}) \frac{\langle n | \hat{c}_1 | m \rangle \langle m | \hat{c}_2^\dagger | n \rangle}{iv - (E_m - E_n)}. \quad (2.6)$$

If we take $1 \equiv 2$, which corresponds to the *local* Green's function, we can introduce the spectral function

$$A_1(v) = \frac{1}{Z} \sum_{mn} e^{-\beta E_n} (1 + e^{-\beta v}) |\langle n | \hat{c}_1 | m \rangle|^2 \delta(v - E_m - E_n), \quad (2.7)$$

where,

$$G_1(iv_n) = \int_{\mathbb{R}} dv \frac{A_1(v)}{iv_n - v}. \quad (2.8)$$

The spectral function $A_1(v)$ is the probability of adding or removing a particle with momentum \mathbf{k}_1 with spin σ_1 from the system. For that reason, $A_1(v)$ is coined the single-particle local density of states. Furthermore, since it represents a probability distribution, the integral over all energies of $A_1(v)$ is equal to 1. It is directly measurable using techniques like angle-resolved photoemission spectroscopy (ARPES), which probes electronic states in the material and reveals electronic structure properties, such as band gaps and quasiparticle dispersions. The peaks in $A_1(v)$ correspond to quasiparticle states, with their position indicating the energy of these states and their width related to the lifetime or decay rate of the quasiparticles. A narrow peak indicates a well-defined quasiparticle with a long lifetime and weak decay rate, while a broad peak suggests the contrary. The spectral function is a key quantity in many-body theory as it connects real-world experimental results to the Green's function formalism, as is shown in the following. By performing analytic continuation in the upper complex plane ($iv \rightarrow v + i0^+$), one can define the retarded Green's function as

$$G_1^R(v) = \int_{\mathbb{R}} dv' \frac{A_1(v')}{v - v' + i0^+}, \quad (2.9)$$

from where one obtains through the Kramers-Kronig relations

$$A_1(v) = -\frac{1}{\pi} \Im G_1^R(v). \quad (2.10)$$

Thus, the spectral function is directly coupled to the imaginary part of the retarded Green's function, connecting many-body theory with physical experiments.

As an example, which will prove itself useful for the future, let us consider non-interacting electrons in a system with translational symmetry that are described by the (Wannier) Hamiltonian

$$\hat{\mathcal{H}}_0 = \sum_{\mathbf{k};12} \varepsilon_{12}(\mathbf{k}) \hat{c}_{\mathbf{k};1}^\dagger \hat{c}_{\mathbf{k};2}, \quad (2.11)$$

where $\varepsilon_{12}(\mathbf{k}) = -\sum_{\mathbf{R};12} t_{12}(\mathbf{R}) e^{i\mathbf{k}\mathbf{R}}$ is the momentum dispersion of the band and is measured with respect to the chemical potential μ . In this case, it is easy to show, that

$$G_{0;12}(v_n, \mathbf{k}) = [iv_n \delta_{12} - \varepsilon_{12}(\mathbf{k})]^{-1}. \quad (2.12)$$

For the one-particle spectral function, we find in this case

$$A_{12}(\varepsilon, \mathbf{k}) = \delta(\varepsilon - \varepsilon_{\mathbf{k};12}), \quad (2.13)$$

corresponding to stable quasiparticles, due to zero width of the quasiparticle peak of $A_{12}(\varepsilon, \mathbf{k})$. The direct computation of the Green's function as expressed in Eq. (??) generally incurs an exponential increase in cost with lattice size for interacting models. As a result, it is common practice to begin with the noninteracting case and construct a perturbative expansion in terms of the interaction around it. In this context, we will start with the non-interacting case described above. This perturbation expansion will not be derived in detail in this thesis, as there are many wonderful resources that explain it thoroughly [something], thus we will only sketch it here. In essence, the expansion is constructed using the so-called S-matrix and employs strategies such as the Wick contraction [wick contraction] and the linked cluster theorem [linked cluster]. The expansion begins by identifying the most general interaction part of the Hamiltonian of Eq. (1.14),

$$\hat{\mathcal{H}}_I = \frac{1}{2} \sum_{1234} U_{1234} \hat{c}_1^\dagger \hat{c}_3^\dagger \hat{c}_4 \hat{c}_2. \quad (2.14)$$

The expansion of the Green's function then reads

$$G_{12}(\tau) = -\frac{1}{\langle S(\beta) \rangle_0} \sum_{n=0}^{\infty} \frac{(-1)^n}{n!} \int_0^\beta d\tau_1 \cdots \int_0^\beta d\tau_n \left\langle \mathcal{T} [\hat{c}_1 \hat{c}_2^\dagger \hat{\mathcal{H}}_I(\tau_1) \cdots \hat{\mathcal{H}}_I(\tau_n)] \right\rangle_0, \quad (2.15)$$

where $S(\beta)$ is the abovementioned S-matrix and $\langle \cdot \rangle_0$ is the thermal expectation value in terms of the non-interacting Hamiltonian $\hat{\mathcal{H}}_0$. In Feynman diagram jargon, this contains all diagrams that are possible, also disconnected ones^[3]. The linked cluster theorem allows us to get rid of those disconnected contributions by effectively cancelling with the $\frac{1}{\langle S(\beta) \rangle_0}$ term in front. This results in

$$G_{12}(\tau) = -\sum_{n=0}^{\infty} \frac{(-1)^n}{n!} \int_0^\beta d\tau_1 \cdots \int_0^\beta d\tau_n \left\langle \mathcal{T} [\hat{c}_1 \hat{c}_2^\dagger \hat{\mathcal{H}}_I(\tau_1) \cdots \hat{\mathcal{H}}_I(\tau_n)] \right\rangle_0^{\text{conn}}, \quad (2.16)$$

where $\langle \cdot \rangle_0^{\text{conn}}$ now indicates that we only consider connected diagrams in the expansion. We can transform this into a diagrammatic representation by applying Wick contractions, which allow us to collect pairs of creation and annihilation operators to form independent expectation values. In the case of the $n = 1$ term in the perturbation expansion of the Green's function,

$$\begin{aligned} G_{1,12}(\tau) = & \sum_{ab\bar{c}\bar{d}} \int_0^\beta d\tau_1 U_{ab\bar{c}\bar{d}} \left[-\left\langle \mathcal{T} [\hat{c}_1(\tau) \hat{c}_a^\dagger(\tau_1)] \right\rangle_0 \left\langle \mathcal{T} [\hat{c}_{\bar{d}}(\tau_1) \hat{c}_{\bar{c}}^\dagger(\tau_1)] \right\rangle_0 \left\langle \mathcal{T} [\hat{c}_b(\tau_1) \hat{c}_2^\dagger(0)] \right\rangle_0 \right. \\ & \left. + \left\langle \mathcal{T} [\hat{c}_1(\tau) \hat{c}_a^\dagger(\tau_1)] \right\rangle_0 \left\langle \mathcal{T} [\hat{c}_b(\tau_1) \hat{c}_c^\dagger(\tau_1)] \right\rangle_0 \left\langle \mathcal{T} [\hat{c}_{\bar{d}}(\tau_1) \hat{c}_2^\dagger(0)] \right\rangle_0 \right]. \end{aligned} \quad (2.17)$$

The remaining expectation values are nothing more than minus the non-interacting Green's function of Eq. (??). Written in Feynman diagrams, the first relevant perturbation expansion term is shown in Fig. ??.

2.2 Self-energy

The one-particle Green's function perturbative expansion is already much simplified in the graphical portrayal. However, the number of diagrams increases exponentially with order n ^[4]. Therefore, the

^[3]Disconnected means, that the term includes a diagram that consists of two separate, disconnected diagrams.

^[4]For $n = 2$ there exist 10 diagrams, for $n = 7$ the number of diagrams is well over a million.

$$G_{1;12}(\tau) = \frac{1}{\tau} \rightarrow \frac{a b}{\tau_1} \rightarrow \frac{2}{0} + \frac{1}{\tau} \rightarrow \frac{a b}{\tau_1} \rightarrow \frac{c d}{\tau_1} \rightarrow \frac{1}{0}$$

FIGURE 2.2: First order diagrams for the single-particle Green's function. The corresponding diagrams are coined the Hartree- and the Fock-term, respectively. As the name suggests, taking only these two diagrams as the whole perturbation expansion leads to the Hartree-Fock approximation, formulated as a diagrammatic theory.

Feynman diagram approach would be of little practical use if the only way to progress was to calculate each diagram one at a time. However, in reality the technique is actually quite useful, since it hints on how to sum up the perturbative series. Let us talk about how it applies to Green's function for single particles. First, let us define another compound index which will further levitate readability. We will set $k = \{\nu, k\}$ and $q = \{\omega, q\}$ as a compound index including momentum and frequency in one index for fermionic (k) and bosonic (q) frequencies and momenta. Note, that if we write ν instead of k , we refer to the *local* part of the quantity with $k = 0$ instead of the *non-local* part.

Diagrams in general can be split up into two classes: (i) diagrams that, by cutting a single internal Green's function line, transform in two lower-order diagrams, which are called one-particle reducible and (ii) diagrams that are not one-particle reducible, which are called one-particle irreducible (1PI). Let us define as the one-particle self-energy Σ_{12}^k the sum of all irreducible diagrams without external legs. For example, the black part of the diagrams in Fig. ?? corresponds to the first-order diagrams of the self-energy. It is then straightforward to rewrite Eq. (??) in terms of the self-energy, yielding

$$G_{12}^k = G_{0;12}^k + \sum_{ab} G_{0;1a}^k \Sigma_{ab}^k G_{b2}^k, \quad (2.18)$$

which results in - when taking Eq. (??) as the noninteracting Green's function and inverting in frequency and momentum space - a way to express the full (interacting) single-particle Green's function in terms of the self-energy

$$G_{12}^k = [i\nu_n \delta_{12} - \varepsilon_{12}(k) - \Sigma_{12}^k]^{-1}. \quad (2.19)$$

Eq. (??) is commonly known as the Dyson equation [**dyson eq**] for the single-particle Green's function and for completeness, its diagrammatic representation can be found in Fig. ???. It is a geometric series, where each term in the sum subsequently adds irreducible diagrams that are pieced together by non-interacting Green's functions to generate all possible diagrams. The self-energy can be obtained by

$$G_{12}^k = \text{bare line } 1 \xrightarrow{k} 2 = \text{bare line } 1 \xrightarrow{k} a \text{ loop } \Sigma_{ab}^k \text{ b } \xrightarrow{k} 2$$

FIGURE 2.3: Diagrammatic representation of Eq. (??). The full Green's function G_{12}^k is drawn as a thick black line.

simply inverting Eq. (??),

$$\Sigma_{12}^k = (G_{0;12}^k)^{-1} - (G_{12}^k)^{-1}. \quad (2.20)$$

Thus, perturbation theory can be done in two distinct ways: the simpler approach is to determine the Green's function directly, for example, up to order n , where the second method is to compute the self-energy up to order n and insert its expression in the Dyson equation Eq. (??). This gives an approximate Green's function containing each order of perturbation theory with only a subset of all possible diagrams. As a result, Eq. (??) represents a way to sum up perturbation theory and is actually more relevant from a physical standpoint. Indeed, many methods leverage the usefulness of this approach, for example the dynamical mean-field theory or the dynamical vertex approximation, as we will see later.

Let us add some physical background to the self-energy in the following. Σ represents the effects of the interaction on the single electron propagators. The real and imaginary part of the self-energy have significant impact on the physical properties of the system. The real part of the self-energy contributes to an energy shift of the electronic states of the single-particle energy levels $\epsilon(\mathbf{k})$ due to interactions. In contrast, the imaginary part of the self-energy is related to the decay or lifetime of quasiparticles and introduces a spectral broadening or damping of the electronic states, indicating how long an excitation or quasiparticle persists before interacting with other excitations or scattering events. A larger imaginary part implies a shorter lifetime and stronger interactions. The first order derivative in frequency, $\frac{\partial \Sigma^k}{\partial \nu}$, contributes to an effective renormalization of the bare electron mass. It also leads to a redistribution of spectral weight in the one-particle spectral function, which provides information about the distribution of energy levels available for excitations. A broader spectral function, whose broadening is controlled by the imaginary part of the self-energy, typically indicates stronger interactions and a more correlated system.

2.3 Two-particle Green's functions

In analogy to the one-particle Green's function, the two-particle Green's function describes the amplitude of the propagation of two particles, two holes or a particle and a hole. A similar expression to Eq. (??) can be formulated for the two-particle Green's function

$$G_{1234}^{qkk'} = -\left\langle \mathcal{T} \left[\hat{c}_{\mathbf{k},1} \hat{c}_{\mathbf{k}-\mathbf{q},2}^\dagger \hat{c}_{\mathbf{k}'-\mathbf{q},3} \hat{c}_{\mathbf{k}',4}^\dagger \right] \right\rangle. \quad (2.21)$$

It describes two particles, two holes or a particle and a hole being inserted in the system at times τ_2 and τ_4 , propagating in the system until they are removed again at τ_1 and τ_3 , respectively. Assuming a stationary Hamiltonian that satisfies time-translation invariance, it is possible to eliminate one imaginary time variable by setting it zero. Then, the Green's function only depends on three time variables and through Fourier transform, also only depends on three frequency and momentum variables. Furthermore, similar to the case for the one-particle Green's function, the absence of spin-orbit coupling reduces the number of spin degrees of freedom

$$G_{\sigma\sigma';1234}^{qkk'} = G_{\sigma\sigma'\sigma'\sigma';1234}^{qkk'} \quad \text{and} \quad (2.22a)$$

$$G_{\overline{\sigma\sigma'},1234}^{qkk'} = G_{\sigma\sigma'\sigma'\sigma';1234}^{qkk'}. \quad (2.22b)$$

In this case, the total incoming and outgoing spin must be equal and this puts a heavy constraint on the possible spin combinations,

$$\sigma_1 = \sigma_2 = \sigma_3 = \sigma_4, \quad (\sigma_1 = \sigma_2) \neq (\sigma_3 = \sigma_4) \quad \text{and} \quad (\sigma_1 = \sigma_4) \neq (\sigma_2 = \sigma_3), \quad (2.23)$$

totaling to only six unique spin combinations, each of which can be seen in Fig. ???. Furthermore, if

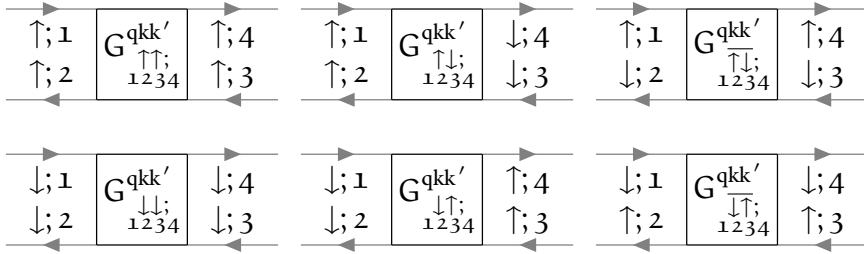


FIGURE 2.4: In the case of absent spin-orbit coupling, these are the only non-vanishing spin combinations of the two-particle Green's function.

one describes quantities in the paramagnetic phase, where the system is SU(2)-symmetric, there are only two independent spin configurations,

$$G_{\sigma\sigma';1234}^{qkk'} = G_{(-\sigma)(-\sigma');1234}^{qkk'} = G_{\sigma'\sigma;1234}^{qkk'} \quad \text{and} \quad (2.24a)$$

$$G_{\sigma\sigma';1234}^{qkk'} = G_{\sigma(-\sigma);1234}^{qkk'} + G_{\sigma(-\sigma);1234}^{qkk'}. \quad (2.24b)$$

For these two spin combinations, the density and magnetic channel specified in the following are a particularly helpful choice of notation, as we shall see in the upcoming sections:

$$G_{d;1234}^{qkk'} = G_{\uparrow\uparrow;1234}^{qkk'} + G_{\uparrow\downarrow;1234}^{qkk'} \quad \text{and} \quad (2.25a)$$

$$G_{m;1234}^{qkk'} = G_{\uparrow\uparrow;1234}^{qkk'} - G_{\uparrow\downarrow;1234}^{qkk'} = G_{\uparrow\downarrow;1234}^{qkk'}. \quad (2.25b)$$

Besides the spin-symmetries discussed above, the Green's function also inherits other properties of the system, such as time-reversal symmetry, which manifests itself by

$$G_{1234}^{qkk'} = G_{\bar{3}421}^{\bar{q}\bar{k}'\bar{k}}, \quad (2.26)$$

where $\bar{k} = \{\nu, -k\}$ is the time-reversed compound momentum variable. Furthermore, the two-particle Green's function satisfies the crossing symmetry, which is a direct manifestation of Pauli's principle. Crossing symmetry refers to the antisymmetric property of the Green's function with respect to the exchange of the incoming and outgoing fermions

$$G_{\sigma\sigma';1234}^{qkk'} = -G_{\sigma'\sigma;3214}^{(k'-k)(k'-q)k'}, \quad (2.27a)$$

$$= -G_{\sigma\sigma';1432}^{(k-k')k(k-q)}, \quad (2.27b)$$

$$= G_{\sigma'\sigma;3412}^{(-q)(k'-q)(k-q)}. \quad (2.27c)$$

The symmetries Eq. (??) - Eq. (??) describe the frequency changes that occur by exchanging the positions of the gray fermion lines, leaving the vertex unchanged. The last line corresponds to a full swap of the incoming and outgoing particle labels. The crossing symmetry is visually shown in Fig. ???. Lastly, the Green's function also possesses symmetry with respect to complex conjugation,

$$(G_{\sigma\sigma';1234}^{qkk'})^* = G_{\sigma'\sigma;4321}^{(-q)(-k)(-k')}. \quad (2.28)$$

At the beginning of the section it was stated that the (four-point) two-particle Green's function only requires three frequency arguments to be fixed since the last one is automatically given by momentum conservation. There are three equivalent choices (coined channels) of independent frequencies (with ν, ν' being a fermionic and ω a bosonic Matsubara frequency)

$$\text{ph-notation: } \{\nu_1 = \nu, \quad \nu_2 = \nu - \omega, \quad \nu_3 = \nu' - \omega, \quad \nu_4 = \nu'\}, \quad (2.29a)$$

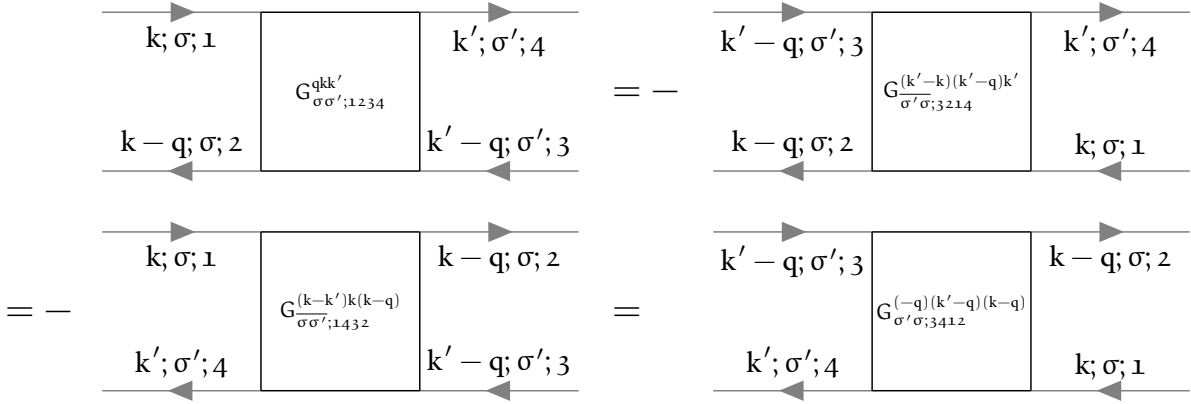


FIGURE 2.5: Diagrammatic representation of the crossing symmetry relations in order of Eq. (??) - Eq. (??).

$\overline{\text{ph}}\text{-notation: } \{v_1 = v, \quad v_2 = v', \quad v_3 = v' - \omega, \quad v_4 = v - \omega\} \quad \text{and} \quad (2.29\text{b})$

$\text{pp-notation: } \{v_1 = v, \quad v_2 = \omega - v', \quad v_3 = \omega - v, \quad v_4 = v'\}. \quad (2.29\text{c})$

To show the effects of this frequency shift and how they affect the labels of the diagrams, we show the two-particle Green's function in the three notations of Eq. (??) - Eq. (??) in Fig. ?? below. Obviously,

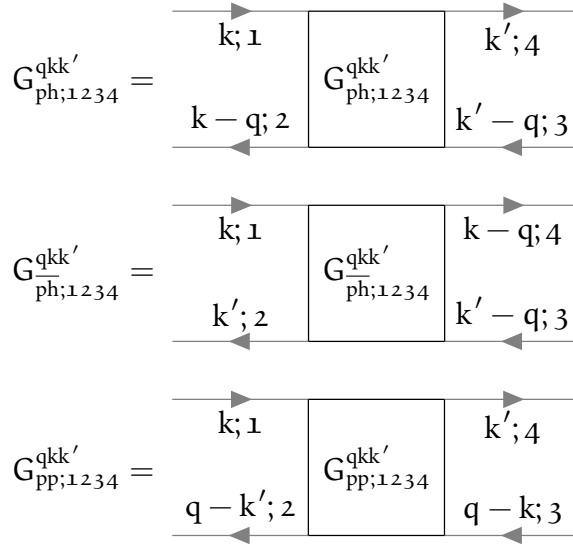


FIGURE 2.6: Two-particle Green's functions in the different frequency notations of Eq. (??) - Eq. (??) expressed in Feynman diagrams. The frequency notation is encoded in an additional subscript, $\{\text{ph}, \overline{\text{ph}}, \text{pp}\}$.

the choice of frequency convention should not have any impact on the physical content of the Green's function, hence it is possible to switch between these channels by applying channel-specific frequency shifts,

$$G_{\text{ph};1234}^{qkk'} = G_{\overline{\text{ph}};1234}^{(k-k')k(k-q)}, \quad (2.30\text{a})$$

$$G_{\overline{\text{ph}};1234}^{qkk'} = G_{\text{ph};1234}^{(k-k')k(k-q)}, \quad (2.30\text{b})$$

$$G_{\text{ph};1234}^{qkk'} = G_{\text{pp};1234}^{(k+k'-q)kk'} \quad \text{and} \quad (2.30\text{c})$$

$$G_{\text{pp};1234}^{qkk'} = G_{\text{ph};1234}^{(k+k'-q)kk'}. \quad (2.30\text{d})$$

Let us finally note that the two-particle Green's function represents all diagrams that are possible that involve two electrons, two holes or an electron and a hole. It can therefore be split into two parts: (i) a part, where the electrons do not interact with each other and propagate independently; and (ii) a part, where the electrons do interact with each other through an infinite number of processes. (ii) is commonly called the connected two-particle Green's function and can be mathematically formulated by

$$G_{\sigma\sigma';1234}^{qkk'} = G_{\sigma\sigma';1234}^{\text{conn};qkk'} + \delta_{q0} G_{\sigma;12}^k G_{\sigma';34}^{k'} - \delta_{\sigma\sigma'} \delta_{kk'} G_{\sigma;14}^k G_{\sigma;32}^{k-q}. \quad (2.31)$$

Diagrammatically, the connected two-particle Green's function contains all diagrams, where two propagating electrons interact with each other. The first terms up to interaction order two are given in Fig. ???. The other terms in Eq. (??) are not that interesting, they merely describe the electrons prop-

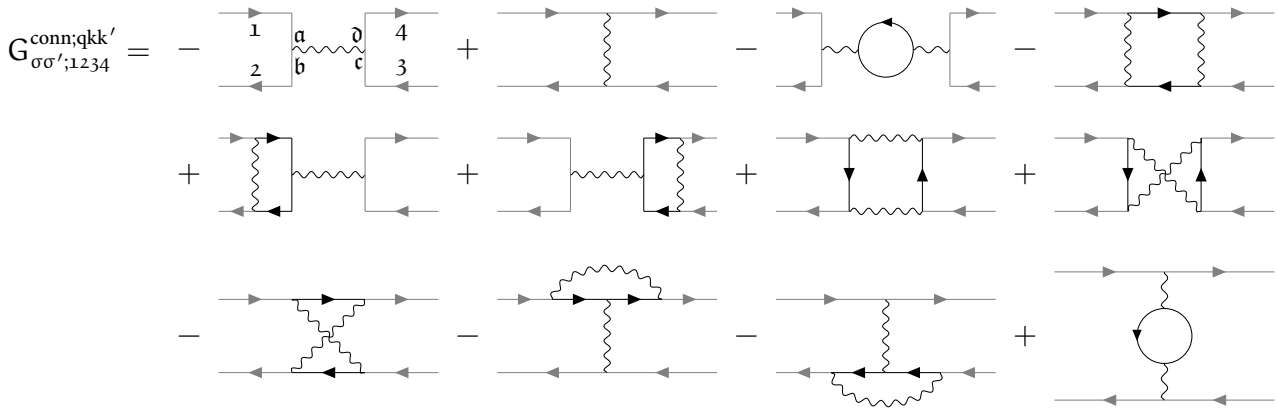


FIGURE 2.7: Diagrammatic representation of the two-particle connected Green's function up to order two. It includes the possible interaction processes that occur between two propagating electrons. The particle labels are only written down for the first diagram, the other diagrams are labeled analogously.

agating in the system without ever interacting with the other. However, we will still show the diagrammatic content of the second and third term of Eq. (??) in Fig. ???. The connected two-particle

$$\delta_{q0} G_{\sigma;12}^k G_{\sigma';34}^{k'} - \delta_{\sigma\sigma'} \delta_{kk'} G_{\sigma;14}^k G_{\sigma;32}^{k-q} = \begin{array}{c} |1 \\ \downarrow \\ 2 \end{array} \delta_{q0} \begin{array}{c} 4 \\ \uparrow \\ 3 \end{array} - \begin{array}{c} 1 \rightarrow 4 \\ \downarrow \\ 2 \leftarrow 3 \end{array} \delta_{\sigma\sigma'} \delta_{kk'}$$

FIGURE 2.8: Disconnected part (second and third term on the right hand side of Eq. (??)) of the two-particle Green's function.

Green's function without the external legs is commonly called the full vertex F , where by convention an additional minus sign is introduced,

$$G_{1234}^{\text{conn};qkk'} = -\frac{1}{\beta} \sum_{ab\bar{c}\bar{d}} G_{1a}^k G_{\bar{b}2}^{k-q} F_{1234}^{qkk'} G_{\bar{3}c}^{k'-q} G_{\bar{d}4}^{k'}. \quad (2.32)$$

By the previous definition, the vertex function $F_{1234}^{qkk'}$ contains all diagrams that connect two incoming and two outgoing lines. All diagrams contained in the full vertex $F_{1234}^{qkk'}$ can be classified by their two-particle reducibility (2PR). A diagram is called two-particle reducible, if it can be split into two separate

parts by cutting two internal Green's function lines. Furthermore, this classification is described by three channels, $\{\text{ph}, \overline{\text{ph}}, \text{pp}\}$, depending on which incoming and outgoing lines are being separated by the “cutting”-process. The ph-channel corresponds to those diagrams, where the sub-parts connect $_{12}$ and $_{34}$, for the ph-channel $_{14}$ and $_{23}$ and for the pp-channel $_{13}$ and $_{24}$ are connected. These reducible diagrams are categorized in $\Phi_{\text{ph};1234}^{\text{qkk}'}$, $\Phi_{\overline{\text{ph}};1234}^{\text{qkk}'}$ and $\Phi_{\text{pp};1234}^{\text{qkk}'}$, respectively. All diagrams that are not two-particle reducible are grouped together in the quantity $\Lambda_{1234}^{\text{qkk}'}$. This procedure is called the Parquet-decomposition and reads mathematically

$$F_{1234}^{\text{qkk}'} = \Lambda_{1234}^{\text{qkk}'} + \Phi_{\text{ph};1234}^{\text{qkk}'} + \Phi_{\overline{\text{ph}};1234}^{\text{qkk}'} + \Phi_{\text{pp};1234}^{\text{qkk}'} \quad (2.33)$$

Another possibility is to split up the full vertex F in reducible and irreducible diagrams in a specific channel $r \in \{\text{ph}, \overline{\text{ph}}, \text{pp}\}$,

$$F_{1234}^{\text{qkk}'} = \Gamma_{r;1234}^{\text{qkk}'} + \Phi_{r;1234}^{\text{qkk}'} \quad (2.34)$$

where $\Gamma_{r;1234}^{\text{qkk}'}$ is the irreducible vertex in channel r and $\Phi_{r;1234}^{\text{qkk}'}$ the corresponding reducible one. Note, that in channel r irreducible diagrams might still be reducible in another channel $r' \neq r$. For example, $\Gamma_{\text{ph};1234}^{\text{qkk}'}$ contains all fully irreducible diagrams, but also all diagrams which are reducible in channels $\overline{\text{ph}}$ and pp ,

$$\Gamma_{\text{ph};1234}^{\text{qkk}'} = \Lambda_{1234}^{\text{qkk}'} + \Phi_{\overline{\text{ph}};1234}^{\text{qkk}'} + \Phi_{\text{pp};1234}^{\text{qkk}'} \quad (2.35)$$

This will be important later in Sec. ??, where we will discuss the Bethe-Salpeter equations. Before that, let us take a look at how one can ease calculations for high frequencies by employing an efficient construction of vertex asymptotics.

2.4 Vertex asymptotics

A full treatment of frequency and momentum dependence of multi-orbital vertex functions severely restricts the speed and memory consumption of numerical calculations. A step towards reducing the computational cost of numerical implementations of equations involving vertex functions, such as the Bethe-Salpeter equations, see Sec. ??, or the Schwinger-Dyson equation, see Sec. ??, thus requires an efficient treatment of the vertex for high Matsubara frequencies. We will see that the vertex - in the high-frequency regime - which originally depended on three independent frequency parameters can be treated as an object with only two frequency dimensions, thus drastically reducing the storage capacity of and ease of calculations including the vertex. In Fig. ??, the frequency dependence of local vertex functions $F_{\text{pp};\uparrow\downarrow}^{\omega\nu\nu'}$, $\Lambda_{\text{pp};\uparrow\downarrow}^{\omega\nu\nu'}$ and $\Phi_{r;\uparrow\downarrow}^{\omega\nu\nu'}$ calculated for the SIAM model are shown for vanishing transfer frequency ω [high-freq asympt]. From this, one can see three very prominent and distinct features of the full vertex F : (i) a constant background that differs from the (local and constant) Hubbard interaction U ; (ii) two diagonal structures, the main ($\nu = \nu'$) and secondary ($\nu = -\nu'$) diagonal and; (iii) a “cross”-like structure along $\nu = \pm \frac{\pi}{\beta}$ and $\nu' = \pm \frac{\pi}{\beta}$. While only shown for the antiparallel spin combination $\uparrow\downarrow$ and vanishing transfer frequency $\omega = 0$, the features are analogous for the parallel spin combination $\uparrow\uparrow$ and for finite ω . These three attributes do *not* decay for high Matsubara frequencies ν and ν' and therefore indicate complex asymptotic behaviour. The individual asymptotic contributions of the fully irreducible vertex Λ and the reducible vertex in channel r to the full vertex F are written in detail in Ref. [high-freq asympt]. Summarized, Λ adds a constant background of size U , Φ_{ph} adds a secondary diagonal structure, $\Phi_{\overline{\text{ph}}}$ adds a diagonal structure and Φ_{pp} adds a constant background and a “cross”-like structure. Notice that this description only refers to the SIAM model

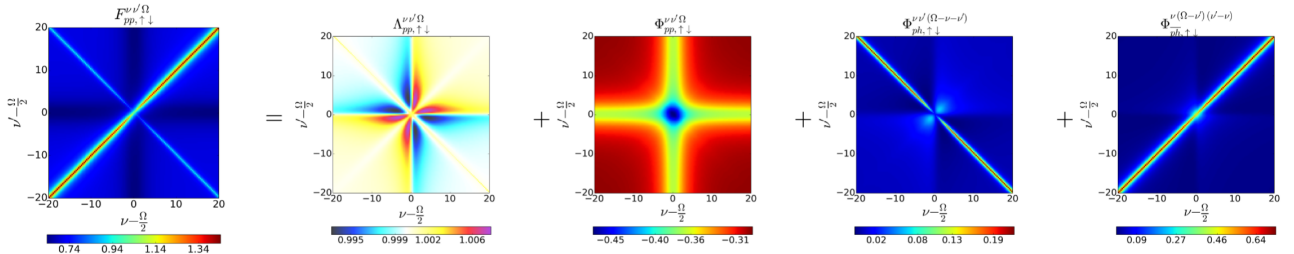


FIGURE 2.9: Numerical SIAM results for all local vertices contained in the Parquet equation Eq. (??) for vanishing transfer frequency $\Omega = 0$, taken from Ref. [high-freq asympt]. In our convention, Ω should be replaced by ω .

and considers solely the one-band case with local quantities and a constant local interaction U . An extension to a multi-orbital formalism and momentum-dependent vertices and interaction U follows naturally and will be discussed in the following.

The asymptotic behaviour for large frequencies of the irreducible vertex $\Gamma_{r;1234;\sigma\sigma'}^{\text{asympt};qkk'}$ follows from the arguments above and reads

$$\Gamma_{ph;1234;\sigma\sigma'}^{\text{asympt};qkk'} = \mathcal{U}_{1234;\sigma\sigma'}^{qkk'}, \quad (2.36)$$

where \mathcal{U} is the non-local Coulomb interaction, written in crossing-symmetric notation

$$\mathcal{U}_{1234;\sigma\sigma'}^{qkk'} = \frac{1}{\beta^2} \left[\underbrace{U_{1324} + V_{1324}^q}_{\beta^2 \mathcal{U}_{1324}^q} - \delta_{\sigma\sigma'} \left(\underbrace{U_{3124} + V_{3124}^{k-k'}}_{\beta^2 \mathcal{U}_{3124}^{k-k'}} \right) \right], \quad (2.37)$$

containing the purely local interaction U and the purely non-local interaction V . From this follows for the irreducible vertex in the density and magnetic channel (in ph-notation)

$$\Gamma_{d;1234}^{\text{asympt};qkk'} = \frac{1}{\beta^2} [2 \mathcal{U}_{1324}^q - \mathcal{U}_{3124}^{k-k'}] \quad \text{and} \quad (2.38a)$$

$$\Gamma_{m;1234}^{\text{asympt};kk'} = -\frac{1}{\beta^2} \mathcal{U}_{3124}^{k-k'}. \quad (2.38b)$$

The procedure for the diagrams reducible in channel r is a bit more involved. A smart choice introduced in Ref. [high-freq asympt] is to classify these diagrams further into three subdivisions, outlined here only briefly:

- Class 1: These are diagrams which connect incoming and outgoing particles only by a single interaction vertex. These diagrams are bubble diagrams and hence only depend on a single bosonic frequency and momentum. The sum of all these diagrams will be encoded in the variable $\mathcal{K}_{r;1234;\sigma\sigma'}^{(1);q}$.
- Class 2: Diagrams corresponding to class 2 are identified by them having either the incoming *or* outgoing particles connected to the same interaction vertex. These diagrams depend on the bosonic transfer frequency and momentum and one fermionic frequency and momentum. The sum of all these diagrams will be encoded in the variables $\mathcal{K}_{r;1234;\sigma\sigma'}^{(2);qk}$ and $\bar{\mathcal{K}}_{r;1234;\sigma\sigma'}^{(2);qk}$, depending on whether the outgoing particles (\mathcal{K}) or the incoming particles ($\bar{\mathcal{K}}$) are connected to the interaction vertex. \mathcal{K} and $\bar{\mathcal{K}}$ are related to each other via time-reversal symmetry, where in the case of a system with additional SU(2)-symmetry corresponds to [rohringer thesis] $\mathcal{K}_{r;1234;\sigma\sigma'}^{(2);qk} = \bar{\mathcal{K}}_{r;1234;\sigma\sigma'}^{(2);qk}$.

- Class 3: These are diagrams where each external Green's function is connected to a different interaction vertex. These diagrams are parametrized by three independent frequency and momentum arguments and are encoded in the “rest” function $\mathcal{R}_{r;1234;\sigma\sigma'}^{qkk'}$.

In the following, we will refer to $\mathcal{K}^{(1)}$, $\mathcal{K}^{(2)}$ and $\bar{\mathcal{K}}^{(2)}$ as kernel functions. One now can - with the help of these classifications - write the reducible Φ_r -vertices as a decomposition of the different kernel functions and the “rest”-function

$$\Phi_{r;1234;\sigma\sigma'}^{qkk'} = \mathcal{K}_{r;1234;\sigma\sigma'}^{(1);q} + \mathcal{K}_{r;1234;\sigma\sigma'}^{(2);qk} + \mathcal{K}_{r;1234;\sigma\sigma'}^{(2);qk'} + \mathcal{R}_{r;1234;\sigma\sigma'}^{qkk'}. \quad (2.39)$$

This composition is *per se* exact. However, to take advantage of this formalism for numerical calculations, one discards the “rest”-function due to its additional frequency dependence entering the inner propagators, resulting in a quicker drop-off in all frequency directions. Thus, the approximation

$$\Phi_{r;1234;\sigma\sigma'}^{\text{asympt};qkk'} \approx \mathcal{K}_{r;1234;\sigma\sigma'}^{(1);q} + \mathcal{K}_{r;1234;\sigma\sigma'}^{(2);qk} + \mathcal{K}_{r;1234;\sigma\sigma'}^{(2);qk'} \quad (2.40)$$

serves as a valid approximation for the high-frequency regime and, in fact, becomes exact for $\nu, \nu' \rightarrow \infty$ [high-freq asympt]. As we can see above, the quantities on the right hand side of Eq. (??) only depend on two Matsubara frequencies instead of three, reducing the numerical complexity and memory usage for Φ_r significantly. This results in a tremendous improvement over a simple truncation in Φ_r for high frequencies. The kernel functions needed to calculate the reducible diagrams can be obtained by [towards ab initio dga]

WAIT, how do i incorporate the non-locality of the interaction \mathcal{U} in the following equations? I guess how I have done it here

$$\mathcal{K}_{r;1234;\sigma\sigma'}^{(1);q} = - \sum_{\substack{ab\\ k_1 k_2; \sigma_1 \sigma_2}} \mathcal{U}_{12ab;\sigma\sigma_1}^{qkk_1} \chi_{r;bacd;c\sigma_1\sigma_2}^{qk_1 k_2} \mathcal{U}_{cd34;\sigma_2\sigma'}^{qk_2 k} \quad \text{and} \quad (2.41)$$

$$\mathcal{K}_{r;1234;\sigma\sigma'}^{(2);qk} = - \sum_{\substack{ab\\ k_1 k_2; \sigma_1 \sigma_2}} F_{r;12ab}^{qkk_1} \chi_{0;bbaab}^{qk_1 k_2} \mathcal{U}_{ba34;\sigma\sigma'}^{qk_2 k} - \mathcal{K}_{r;1234;\sigma\sigma'}^{(1);q}, \quad (2.42)$$

where $\mathcal{K}^{(1)}$ is subtracted to account for double-counting of diagrams. The density and magnetic contributions of the kernel functions read

$$\mathcal{K}_{d;1234}^{(1);q} \quad (2.43)$$

$$\mathcal{K}_{m;1234}^{(1);q} \quad (2.44)$$

$$\mathcal{K}_{d;1234}^{(2);qk} \quad (2.45)$$

$$\mathcal{K}_{m;1234}^{(2);qk} \quad (2.46)$$

PUT AT END OF SECTION Before that, let us briefly introduce the concept of linear response and the central physical property describing the response of a system with respect to an external perturbation^[5], the susceptibility.

2.5 Susceptibility

Experimentally, it is not possible to directly extract information (just by “looking”) about the interactions between electrons in a system. Instead, in spectroscopic experiments, a perturbation is applied

^[5]For example an external electromagnetic field.

to the system and one measures the system's response. In particular, one measures how expectation values $\langle \cdot \rangle$ of operators (take the multi-dimensional operator $\hat{O}_i(\tau)$ as an example) changes when an external field $h_j(\tau)$ is applied. In linear response theory, this response is - as the name suggests - taken to be linear in the perturbing field, requiring this field to be sufficiently small in order for this description to be a good approximation,

$$\langle \hat{O}_i(\tau) \rangle_h - \langle \hat{O}_i(\tau) \rangle_{h=0} = \int_0^\beta d\tau' \chi_{ij}(\tau - \tau') h_j(\tau') + \mathcal{O}(h^2), \quad (2.47)$$

where $\chi_{ij}(\tau - \tau')$ is coined physical susceptibility and does not depend on the field $h_j(\tau)$. $\chi(\tau - \tau')$ fulfills the Kramers-Kronig relations, is causal ($\chi_{ij}(\tau - \tau') = \Theta(\tau - \tau')\chi_{ij}(\tau - \tau')$) and is finite ($\forall \tau, \tau' : \exists C \in \mathbb{R} : |\chi_{ij}(\tau - \tau')| < C$). The susceptibility can be computed straightforwardly by taking the functional derivative of $\hat{O}_i(\tau)$ with respect to the field $h_j(\tau)$,

$$\chi_{ij}(\tau - \tau') = \left. \frac{\delta \langle \hat{O}_i(\tau') \rangle}{\delta h_j(\tau)} \right|_{h=0} = \langle T \hat{O}_i(\tau) \hat{O}_j(\tau') \rangle - \langle \hat{O}_i \rangle \langle \hat{O}_j \rangle. \quad (2.48)$$

On the two-particle level, only the density's response to variations in the one-particle energy, χ_d , and the magnetization's response to variation in the electromagnetic field in the same direction, χ_m , are non-zero

$$\chi_d(\tau) = \chi_{nn}(\tau) = -\left. \frac{\delta \langle \hat{n} \rangle}{\delta \mu(\tau)} \right|_{\mu=0} \quad \text{and} \quad (2.49a)$$

$$\chi_m(\tau) = \chi_{ii}(\tau) = \left. \frac{\delta \langle \hat{\sigma}_i \rangle}{\delta h_i(\tau)} \right|_{h=0}, \quad (2.49b)$$

where $i \in \{x, y, z\}$. The physical susceptibilities are included in the two-particle Green's function, as we will see shortly. In fact, the sum of terms corresponding to the two disconnected, horizontal Green's function lines and the vertex part is denoted as the general susceptibility and can be expressed as

$$\begin{aligned} \chi_{1234}^{qkk'} &= \beta \left(G_{1234}^{qkk'} - \delta_{q0} G_{12}^k G_{34}^{k'} \right) \\ &= -\beta \delta_{kk'} G_{14}^k G_{32}^{k-q} - \sum_{ab\bar{c}\bar{d}} G_{1a}^k G_{b2}^{k-q} F_{ab\bar{c}\bar{d}}^{qkk'} G_{3\bar{c}}^{k'-q} G_{\bar{d}4}^{k'} \\ &= \chi_{0;1234}^{qkk} - \frac{1}{\beta^2} \sum_{ab\bar{c}\bar{d}} \chi_{0;12\bar{b}a}^{qkk} F_{ab\bar{c}\bar{d}}^{qkk'} \chi_{0;\bar{d}\bar{c}34}^{qk'k'}, \end{aligned} \quad (2.50)$$

where

$$\chi_{0;1234}^{qkk'} = -\beta G_{14}^k G_{32}^{k'-q} \quad (2.51)$$

is commonly denoted as the generalized bubble susceptibility. From this one can obtain physical susceptibilities by contracting the inner legs, i.e.,

$$\chi_{14}^q = \sum_{kk';23} \chi_{1234}^{qkk'}. \quad (2.52)$$

The diagrammatic content of the physical susceptibility is shown in Fig. ?? below. Similarly, the contracted bubble susceptibility can be written as

$$\chi_{0;14}^q = \sum_{kk';23} \chi_{0;1234}^{qkk'}. \quad (2.53)$$

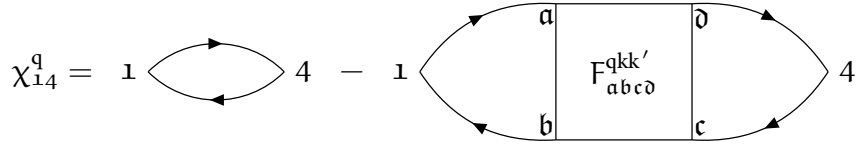


FIGURE 2.10: The physical susceptibility is equal to the generalized susceptibility with contracted legs, see Eq. (??).

Similarly to Eq. (??) and Eq. (??), one can write down density and magnetic spin combinations,

$$\chi_d^q = \chi_{\uparrow\uparrow}^q + \chi_{\uparrow\downarrow}^q = \chi_{\downarrow\downarrow}^q \quad \text{and} \quad (2.54a)$$

$$\chi_m^q = \chi_{\uparrow\uparrow}^q + \chi_{\uparrow\downarrow}^q. \quad (2.54b)$$

Note that expressions Eq. (??) and Eq. (??) are nothing more than the Fourier transformed versions of Eq. (??) and Eq. (??), respectively.

2.6 Bethe-Salpeter equation

In the section above we have specified $\Gamma_{r;1234}^{qkk'}$ as the fully irreducible vertex in channel r and $\Phi_{r;1234}^{qkk'}$ as the reducible diagrams in channel r . We can now construct the full set of $\Phi_{r;1234}^{qkk'}$ from the irreducible vertex by chaining them together with two green's function lines connecting two irreducible vertices. This results in so-called ladders,

$$\Phi_{r;1234}^{qkk'} = \sum_{k_1;abc} \Gamma_{r;12ab}^{qkk_1} G_{bc}^{k_1} G_{da}^{k_1-q} \Gamma_{r;cd34}^{qk_1 k'} \quad (2.55)$$

$$+ \sum_{\substack{k_1 k_2; abc \\ efg}} \Gamma_{r;12ab}^{qkk_1} G_{bc}^{k_1} G_{da}^{k_1-q} \Gamma_{r;cdef}^{qk_1 k_2} G_{fg}^{k_2} G_{he}^{k_2-q} \Gamma_{r;gh34}^{qk_2 k'} + \dots \quad (2.56)$$

By combining Eq. (??) and Eq. (??), one can obtain the Bethe-Salpeter equation in channel r ,

$$\Gamma_{r;1234}^{qkk'} = \Gamma_{r;1234}^{qkk'} - \frac{1}{\beta} \sum_{k_1;abc} \Gamma_{r;12ba}^{qkk_1} \chi_{0;abc}^{qk_1 k_1} \Gamma_{r;dc34}^{qk_1 k'} \quad (2.57)$$

where we have expressed the full vertex $\Gamma_{r;1234}^{qkk'}$ in terms of the irreducible vertex $\Gamma_{r;1234}^{qkk'}$ and the bare (bubble) susceptibility. This

Combining in the previous section derived equations Eq. (??) and Eq. (??), it is possible to write the full vertex as a Dyson-like equation with the generalized susceptibility, reading

$$\Gamma_{r;1234}^{qkk'} = \Gamma_{r;1234}^{qkk'} + \Phi_{r;1234}^{qkk'} = \Gamma_{r;1234}^{qkk'} + \sum_{k'';abc} \Gamma_{r;12ba}^{qkk''} \chi_{0;abc}^{qk'' k''} \Gamma_{r;dc34}^{qk'' k'}, \quad (2.58)$$

where $r \in \{d, m\}$ denotes the (d)ensity or (m)agnetic spin combination, which for the irreducible and full vertex, Γ and Γ , respectively, is similar to that for χ , see Eq. (??) and Eq. (??).

CHAPTER 3

QUANTUM MANY-BODY METHODS

CHAPTER 4

APPLICATION AND CALCULATION

CHAPTER 5

RESULTS

CHAPTER 6

OUTLOOK

6.1 Hubbard Model

Lorem ipsum dolor sit amet, consectetur adipiscing elit. Sed in dolor eu arcu ultricies vulputate in in quam. Mauris vel tellus quis velit feugiat laoreet non nec tortor. Proin justo nunc, vulputate eu massa id, ornare sagittis ante. Nunc pellentesque commodo dolor, vitae vehicula lectus lobortis in. Morbi ultricies eros pellentesque interdum malesuada. Donec a finibus libero. Donec quis feugiat mi. Nunc bibendum, ex vitae porttitor tempus, arcu justo ullamcorper ligula, eu viverra arcu sapien ac ante. Nam feugiat arcu pharetra efficitur accumsan. Quisque id dui in tortor vulputate tincidunt. Morbi sit amet sapien in tortor finibus tristique. Curabitur in eros orci. Curabitur eget commodo dui.

$$\mathcal{C} = \mathcal{M} = C = \int_{\mathbb{R}}^{\infty} dx e^{ikx} \mathbf{1}_{234} \mathcal{U}(\mathbf{R}_1, \mathbf{R}_2). \quad (6.1)$$

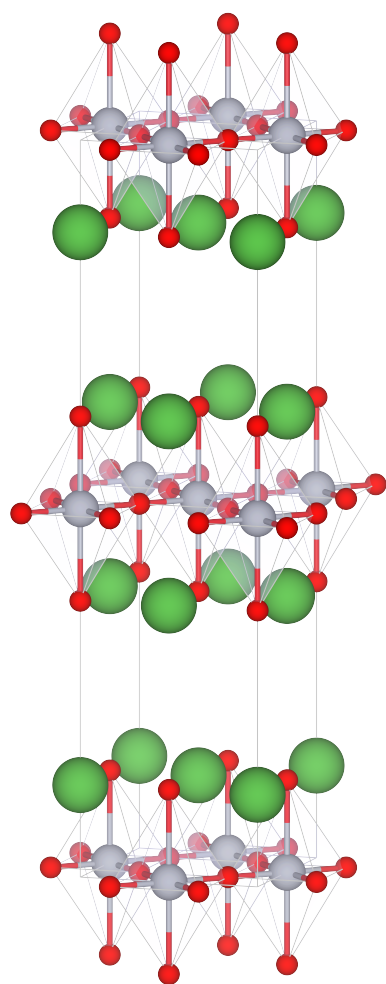


FIGURE 6.1: Test